Nanoscale

Royal Society of Chemistry

Adsorbate-induced structural evolution changes the mechanism of CO oxidation on a Rh/Fe₃O₄(001) model catalyst†

Zdenek Jakub, [a] Jan Hulva,[a] Paul T. P. Ryan, [b,c] David A. Duncan, [b]
David J. Payne,[c] Roland Bliem, [a] Manuel Ulreich,[a] Patrick Hofegger,[a]
Florian Kraushofer, [a] Matthias Meier,[a,d] Michael Schmid, [a] Ulrike Diebold [a]
and Gareth S. Parkinson [*a]

The structure of a catalyst often changes in reactive environments, and following the structural evolution is crucial for the identification of the catalyst's active phase and reaction mechanism. Here we present an atomic-scale study of CO oxidation on a model Rh/Fe₃O₄(001) "single-atom" catalyst, which has a very different evolution depending on which of the two reactants, O_2 or CO, is adsorbed first. Using temperature-programmed desorption (TPD) combined with scanning tunneling microscopy (STM) and X-ray photoelectron spectroscopy (XPS), we show that O_2 destabilizes Rh atoms, leading to the formation of Rh_xO_y clusters; these catalyze CO oxidation via a Langmuir–Hinshelwood mechanism at temperatures as low as 200 K. If CO adsorbs first, the system is poisoned for direct interaction with O_2, and CO oxidation is dominated by a Mars-van-Krevelen pathway at 480 K.

Introduction

Supported rhodium catalysts show high activity for a number of reactions, including CO oxidation.[1–4] It is generally accepted that Rh nanoparticles supported on rigid, irreducible substrates catalyze CO oxidation via the Langmuir–Hinshelwood (L–H) or Eley–Rideal (E–R) mechanisms, where the CO and O_2 molecules either coadsorb on the surface (L–H), or one of the molecules reacts directly from the gas phase with the other molecule adsorbed on the surface (E–R).[6–12] However, the reactivity of the system is often affected by the choice of support, and reducible supports enable an alternative pathway, the so-called Mars-van-Krevelen (MvK) mechanism. Here, oxygen is extracted from the metal oxide lattice to oxidise CO, and the lattice is repaired by O_2 from the gas phase.[14,16–19] Metal–support interactions are not always beneficial, however, and encapsulation by the support can completely deactivate the catalyst.[13,14,20,21]

Improving a catalyst's activity, selectivity, and stability requires the optimization of atomic-scale processes that are very difficult to ascertain on working catalysts. This motivates the use of well-defined model systems studied by the surface science approach, which can provide atomic-scale insights.

In this paper we present how CO oxidation proceeds on a Rh/Fe₃O₄(001) model "single-atom" catalyst. Using a combination of temperature-programmed desorption (TPD), scanning tunneling microscopy (STM), and X-ray photoelectron spectroscopy (XPS), we show the system is active for CO oxidation by both L–H and MvK mechanisms, depending on which of the reactants the surface is exposed to first. Oxygen adsorption leads to formation of superoxo $(O_2)^-$ species bound to Rh_1 adatoms, which rapidly agglomerate to small Rh_xO_y clusters. The clusters contain weakly bound oxygen, which reacts with CO below room temperature. In contrast, CO adsorption on the bare Rh_1 species poisons the system for O_2 adsorption, but CO oxidation nevertheless takes place via a MvK mechanism at ca. 480 K. Two different deactivation mechanisms are observed: the oxidised clusters become inactive after the first desorption of the weakly bound oxygen, while the Rh_1 adatoms incorporate into the support lattice as the CO desorbs.

ᵃInstitute of Applied Physics, TU Wien, 1040 Vienna, Austria.
E-mail: parkinson@iap.tuwien.ac.at
ᵇDiamond Light Source, Harwell Science and Innovation Campus, Didcot, OX11 0DE, UK
ᶜDepartment of Materials, Imperial College London, South Kensington, London, SW7 2AZ, UK
ᵈUniversity of Vienna, Faculty of Physics and Center for Computational Materials Science, 1090 Vienna, Austria
†Electronic supplementary information (ESI) available. See DOI: 10.1039/c9nr10087c

Methods

The experiments were carried out using two independent ultra-high vacuum (UHV) setups. The STM data were acquired

in a two-vessel UHV chamber consisting of a preparation chamber ($p < 10^{-10}$ mbar) and an analysis chamber ($p < 7 \times 10^{-11}$ mbar) equipped with an Omicron μ-STM operated at room temperature in constant-current mode with electrochemically etched tungsten tips. The chamber further includes commercial XPS, Auger electron spectroscopy and low-energy electron diffraction instruments. The STM images were corrected for distortion and creep of the piezo scanner as described in ref. 22.

The TPD and XPS data were acquired in a second chamber equipped with a liquid-He cryostat, a home-built molecular beam source, a quadrupole mass spectrometer (Hiden HAL 3F PIC), a monochromatized Al/Ag twin anode X-ray source (Specs XR50 M, FOCUS 500), a hemispherical analyzer (Specs Phoibos 150), a low-energy electron diffraction setup (Specs ErLEED), an ion source (Specs IQE 12/38) and a UV source (Specs UVS 10/35). This chamber was specifically designed for surface chemistry studies of single-crystal oxide samples; full details are given in ref. 23. The samples were mounted on a Ta sample plate using Ta clips, with a thin Au foil placed between the sample plate and the sample to ensure good thermal contact. The sample plate was attached to the liquid-He cryostat via Ta rods, and the temperature was measured by a K-type thermocouple spot-welded on the sample plate. A molecular beam is formed by expansion of 0.53 mbar $^{18}O_2$ or 0.27 mbar ^{13}CO through two differentially pumped stages. This results in a well-defined beam spot on the sample surface with a diameter of 3.35 ± 0.17 mm and a top-hat intensity profile.[23] The TPD spectra were acquired with a 1 K s^{-1} heating ramp.

All the experiments were conducted on natural $Fe_3O_4(001)$ single crystals (SurfaceNet GmbH or Surface Preparation Laboratory) prepared by sputtering (1 keV Ar$^+$ or Ne$^+$, 10 min) and annealing in UHV (930 K, 10 min). Every other annealing step was done in a partial pressure of O_2 ($p_{O_2} = 5 \times 10^{-7}$ mbar, 20 min) to avoid reduction of the surface. Rhodium was deposited using Focus e-beam evaporators, and the deposition rate was calibrated by temperature-stabilized quartz crystal microbalances (QCM). One monolayer (ML) is defined as one atom per ($\sqrt{2} \times \sqrt{2}$)R45° unit cell of the $Fe_3O_4(001)$, which corresponds to 1.42×10^{14} atoms per cm^2.

Results

Rh_1 species on $Fe_3O_4(001)$

Fig. 1a and b shows STM images of the $Fe_3O_4(001)$ surface before and after deposition of Rh. The undulating rows running in the [$\bar{1}10$] direction correspond to 5-fold co-ordinated Fe atoms in surface octahedral sites (Fe_{oct}, see model in the inset of Fig. 1a). In each pair of neighbouring terraces, the surface Fe_{oct} row direction is rotated by 90°, as expected for the spinel structure (not shown here). Surface oxygen atoms are not visible in the STM images because they possess no density of states near the Fermi level, but their positions are precisely known from diffraction studies and density functional theory calculations.[24,25] This $Fe_3O_4(001)$ surface reconstruction is based on subsurface cation vacancies (therefore it's referred to as the SCV reconstruction), and it has
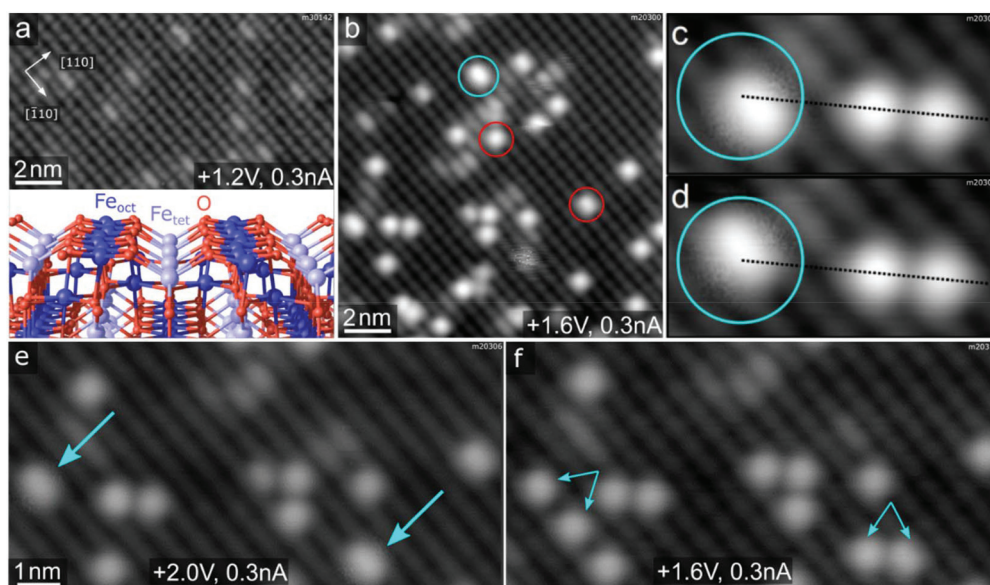

Fig. 1 Characterization of the Rh/$Fe_3O_4(001)$ system by STM. (a) STM images of pristine $Fe_3O_4(001)$ surface show undulating rows of Fe_{oct} running in the [$\bar{1}10$] direction. The small bright species on the Fe_{oct} rows are surface hydroxyls.[5] The inset shows a model of the $Fe_3O_4(001)$ surface with the octahedral Fe_{oct}, tetrahedral Fe_{tet} and O atoms being represented by dark blue, light blue and red spheres, respectively. (b) After deposition of 0.2 ML Rh at room temperature, the majority species are Rh_1 adatoms (red circles), but we also observe slightly elongated species which we identify as Rh_2 dimers (cyan circles). (c and d) The Rh_2 dimers exhibit characteristic hopping motion in subsequent STM images (broken lines for guidance). (e and f) Scanning with a +3 V bias results in dissociation of the Rh_2 dimers (cyan arrows in panel e) into pairs of single Rh_1 adatoms (paired cyan arrows in panel f). The +3 V scan was done between acquisition of images shown in (e) and (f).

been shown previously to support dense arrays of single metal atoms, preventing the adatom mobility and cluster formation even at elevated temperatures.[15,24,26–28] This is due to the existence of highly stable adsorption sites with a nearest-neighbour distance of 0.84 nm, in which the adatoms are 2-fold co-ordinated to the surface oxygen atoms, essentially occupying a bulk continuation tetrahedral site (schematic representation shown in the uppermost inset of Fig. 2a). After deposition of Rh at room temperature, isolated Rh_1 adatoms appear as bright protrusions (red circles in Fig. 1b) sitting between the Fe_{oct} rows. In addition to the single Rh_1 adatoms, we also observe larger elongated species (cyan circle in Fig. 1b), which in subsequent STM scans exhibit a distinctive hopping motion over the adsorption site (Fig. 1c and d). We identify these species as metastable Rh_2 dimers that can be split into two Rh_1 adatoms by bias pulsing or high-bias scanning. Fig. 1e and f shows this process on two STM images acquired on the same spot: in Fig. 1e two Rh_2 dimers are observed (cyan arrows), Fig. 1f shows pairs of isolated Rh_1 adatoms (smaller paired arrows) appearing instead of the Rh_2 after the surface was scanned with a +3 V bias. The observed hopping of the Rh_2 is restricted to the given adsorption site, thus it might be also considered a restructuring of the dimer and does not lead to destabilization of the system by diffusion or agglomeration. Apart from the dimer hopping, no mobility of Rh species is observed in subsequently acquired STM images at room temperature under UHV conditions. The $Fe_3O_4(001)$ surface supports the Rh_1 adatoms even at significantly higher coverages; Fig. S1† shows an STM image of 0.5 ML $Rh/Fe_3O_4(001)$ featuring a high density of Rh_1 adatoms, and XPS spectra acquired on an $Fe_3O_4(001)$ surface with varying Rh coverage between 0.1

and 0.8 ML Rh showing virtually no difference in Rh 3d peak shape or position.

At elevated temperatures, the Rh_1 adatoms are unstable against incorporation into the $Fe_3O_4(001)$ support. Such a phenomenon has been observed for several different metal adatoms on $Fe_3O_4(001)$ before and the foreign adatom can either substitute a 5-fold coordinated surface Fe_{oct} or incorporate in the vacant octahedral site of the SCV reconstruction.[13–15,29] Schematic representations of the three possible sites of Rh_1 near the surface are shown in insets in Fig. 2a. The incorporation of Rh takes place at temperatures above ≈450 K and can be followed both in STM and XPS, as shown in Fig. 2a and b. STM images taken after annealing to 500 K show predominantly elongated (orange circle) and circular (purple circle) features on the Fe_{oct} rows, which is consistent with Rh_1 incorporated into the subsurface 6-fold site or surface 5-fold site, respectively (STM simulations of different metal adatoms in the same sites are provided in ref. 14, 15 and Fig. S2†). Additionally, we observe an increased number of bigger brighter features, presumably Rh clusters, and a very small number of remaining 2-fold Rh_1 adatoms (red circle). Fig. 2b shows the Rh 3d region of XPS spectra taken after depositing 0.6 ML Rh and heating to different temperatures. After deposition at 300 K, the Rh 3d peak maximum is located at ≈307.7 eV, but its broad shape suggests convolution of several components. Apart from the main signal corresponding to 2-fold Rh_1, the additional XPS components might come from the Rh_2 dimers or Rh_1 adatoms residing in the vicinity of surface defects or step edges. On different samples, small variations of the peak maximum between 307.7 and 308.1 eV were observed, most likely depending on the relative
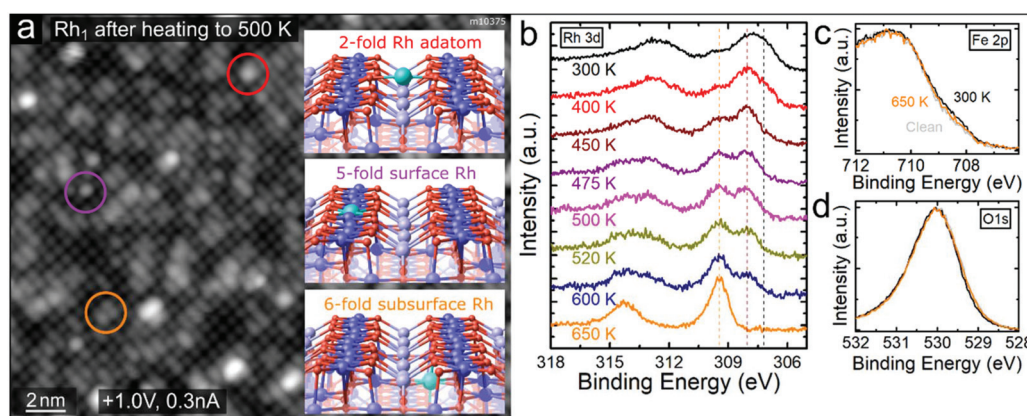

Fig. 2 Rh_1 adatoms incorporate into the $Fe_3O_4(001)$ support upon annealing above 450 K. (a) STM images after deposition of 0.4 ML Rh and heating to 500 K show predominantly circular protrusions (highlighted by purple colour) and elongated protrusions (orange colour) on the Fe_{oct} rows. Only a very small number of Rh_1 remain in the 2-fold coordinated site between the Fe_{oct} rows (red colour). We identify the new species as Rh_1 incorporated in the octahedral cation sites near the surface, consistent with previously reported studies of various metal adatoms on $Fe_3O_4(001)$.[14,15] Schematic representations of these sites are shown in the insets and labelled with the color of the corresponding circle. (b) Rh 3d region of the XPS spectra (monochromated Al Kα, grazing emission) taken after heating to different temperatures (measured after cooling back to 300 K). Upon heating to 400 K the Rh 3d peak maximum shifts to 308.0 eV, as the low binding-energy shoulder at 307.2 eV decreases. Heating above 450 K leads to an increase of the 309.5 eV component, which becomes dominant above 600 K. We attribute this component to Rh incorporated into the octahedral sites of the $Fe_3O_4(001)$ surface. (c and d) The Fe 2p and O 1s peaks corresponding to the first and last spectra shown in (b). Notably, in the Fe 2p region the shoulder at ≈708.5 eV slightly increases upon Rh deposition, indicating an increased amount of Fe^{2+} near the surface. This shoulder decreases again upon heating as the Rh cations diffuse into deeper layers.

number of these species. After heating to 400 K we observe a decrease on the low-binding-energy side of the peak (around ≈307.2 eV) and the peak maximum shifts to 308.0 eV. Heating above 450 K leads to an increase of a higher-binding-energy component at 309.5 eV and decrease of the signal at 308.0 eV. After heating to 650 K, the 308.0 eV peak is no longer observed, and the 309.5 eV component is dominant. Prolonged heating above this temperature leads to a decrease and eventual disappearance of the Rh signal in XPS, consistent with diffusion of Rh into the Fe_3O_4 bulk (Fig. S3†). Thus, we attribute the 309.5 eV component to Rh incorporated into the $Fe_3O_4(001)$ substrate.

The Fe 2p and O 1s regions only show small differences with Rh deposition and heating (Fig. 2c and d). Upon Rh deposition, an Fe 2p shoulder at ≈708.5 eV slightly increases in comparison to the clean surface, indicating an increased amount of Fe^{2+} near the surface.[30] This shoulder decreases again upon heating, presumably because the Rh incorporates and thus the number of near-surface cations decreases.

Exposing Rh_1/$Fe_3O_4(001)$ to O_2

When the Rh_1/$Fe_3O_4(001)$ system is exposed to O_2 at room temperature, the Rh_1 adatoms become mobile and begin to agglomerate. Fig. 3a–c shows three frames of an STM movie acquired while keeping a constant background pressure of 2×10^{-10} mbar O_2 in the analysis chamber. Single adatoms (highlighted by red circles) form well-resolved oxidised Rh_2O_x dimers (yellow rectangles) and subsequently bigger Rh_xO_y clusters (purple rectangle). Over the course of the STM movie, no O_2 adsorption was observed on the Rh_2 dimers (cyan circle).
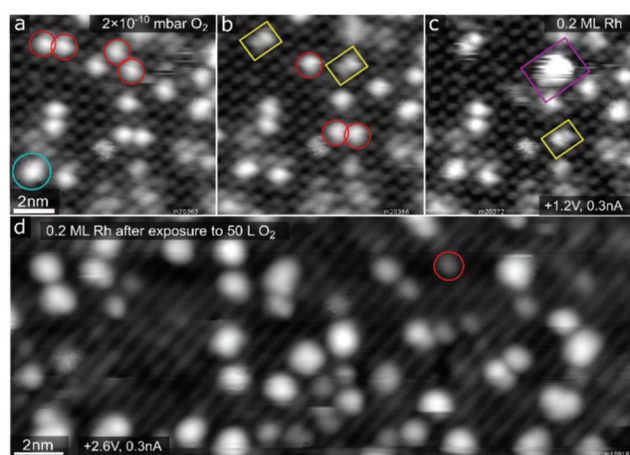
After dosing a higher amount of O_2 in the preparation chamber (50 Langmuir, where 1 L = 1.33×10^{-6} mbar s), the majority species observed in STM are small Rh_xO_y clusters, although some adatoms remain (Fig. 3d). Scanning of the oxidised Rh_xO_y species is difficult because the tip is very unstable, with frequent tip changes suggesting the presence of weakly bound species that interact with the STM tip. A comparison of the cluster density following saturation exposure with the initial adatom coverage suggests that the majority contain at most 2–3 Rh atoms. The fact that similar Rh agglomeration was observed after O_2 exposure in the preparation chamber suggests that the mobility observed in STM movies is not solely tip-induced. After heating the surface with oxidised Rh_xO_y clusters to 400 K, no structural differences are observed, but the imaging becomes much more stable, suggesting desorption or trapping of the weakly bound species.

Fig. 4a shows O_2 TPD measurements from the clean $Fe_3O_4(001)$ surface (grey curve) and from the surface with 0.6
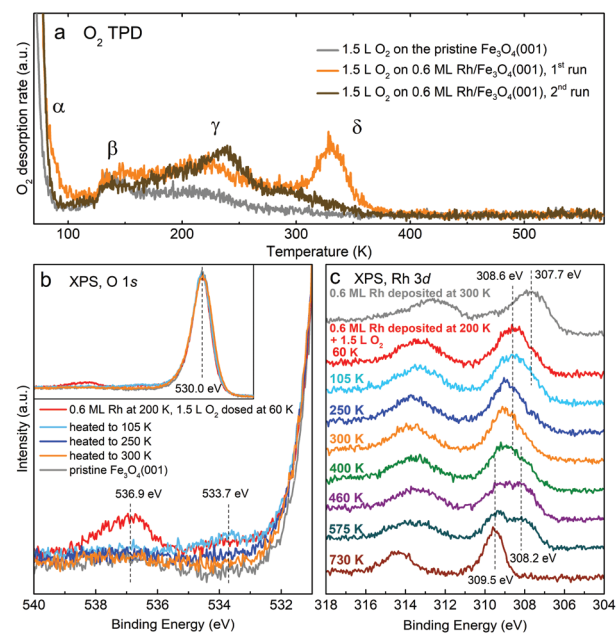

Fig. 4 Spectroscopic characterization of O_2 adsorption on Rh/$Fe_3O_4(001)$ by TPD and XPS. In all spectra, 1.5 L O_2 was dosed at 60 K. (a) O_2 TPD spectra acquired in the first (orange curve) and second (brown curve) dosing on 0.6 ML Rh/$Fe_3O_4(001)$. Notably, the δ peak at ≈330 K appears only in the first dosing experiment. Reference spectra of the clean surface are plotted in grey. (b and c) Details of the O 1s and Rh 3d XPS regions (monochromatized Al Kα, grazing emission) of 0.6 ML Rh/$Fe_3O_4(001)$ after O_2 dosing and heating to different temperatures. Compared to the pristine $Fe_3O_4(001)$, we identify two new components in the O 1s region at 533.7 and 536.9 eV. The spectra taken after heating above room temperature look identical to the orange curve taken at 300 K. The whole O 1s region is shown in the inset in (b). (c) Adsorption of O_2 at 60 K causes a ≈0.9 eV shift of the Rh 3d peak, and a further shift is observed upon heating to 300 K. Heating above ≈500 K leads to growth of the 309.5 eV component corresponding to Rh incorporated into the substrate. Up to 300 K, the spectra were taken at the temperatures given; for higher temperatures, the spectra were taken after cooling the sample back to 300 K.

Fig. 3 STM of Rh_1/$Fe_3O_4(001)$ and its interaction with oxygen. (a–c) Three frames from an STM movie acquired while keeping a constant O_2 background pressure of 2×10^{-10} mbar. Panel (a) shows a majority of single Rh_1 adatoms (red circles). During the O_2 exposure these species first form well-resolved Rh_2O_x clusters (yellow rectangles in panels (b) and (c)) and subsequently bigger nanoparticles (purple rectangle in panel (c)). (d) After a high dose (50 L) of O_2 at room temperature the imaging becomes unstable, and the majority species are larger bright clusters of varying size and shape. A few Rh_1 adatoms remain; one of them is highlighted by the red circle.

ML Rh (orange and brown curves). On the pristine $Fe_3O_4(001)$ surface, O_2 physisorbs below 70 K (desorption peak labelled α in Fig. 4a, full spectrum shown in Fig. S4†), but in our work this phase could not be saturated due to the O_2 dosing temperature (60 K) being within this desorption peak. Thus, desorption already takes place before the start of the heating ramp and the magnitude and shape of the α peak varies in repeated measurements due to slightly varying time between dosing and heating. Above 100 K, the O_2 TPD acquired on the pristine surface exhibits two distinct peaks, labelled β and γ in Fig. 4a and Fig. S4,† which presumably correspond to desorption from defects, domain boundaries, and/or step edges. The presence of Rh_1 adatoms on the surface prior to O_2 dosing leads to an increase of these two desorption peaks and induces a sharp new desorption peak, δ, at ≈330 K. When the TPD measurement was repeated on the same sample (following termination of the previous heating ramp at 570 K), the δ peak was no longer present (brown curve in Fig. 4a), and a similar result was observed in a separate experiment when the first heating ramp ended already at 380 K, before any Rh incorporation took place (evidenced by XPS spectra).

XPS characterization of the O_2 adsorption on $Rh/Fe_3O_4(001)$ is shown in Fig. 4b and c. Spectra taken directly after Rh deposition at 200 K and dosing 1.5 L O_2 at 60 K reveal two new components in the O 1s region at 533.7 and 536.9 eV (red curve in Fig. 4b). The 536.9 eV signal quickly decreases over time and completely disappears within several minutes, which is consistent with the O_2 physisorbed on $Fe_3O_4(001)$ and readily desorbing at 60 K. The 533.7 eV component remains unchanged upon heating to 105 K, but disappears upon heating above 250 K (blue and orange curves in Fig. 4b). After heating to 300 K (orange curve), the spectrum in the O 1s region closely resembles the spectrum acquired on a pristine $Fe_3O_4(001)$ surface (grey curve), save for a very small and broad shoulder between 530–535 eV, which can be attributed to a small amount of water adsorbed on surface defects.[31] Upon heating to higher temperatures up to 730 K, no significant change is observed in the O 1s region.

The adsorption of O_2 can also be followed in the Rh 3d region. Fig. 4c shows spectra taken after Rh deposition (0.6 ML),

dosing O_2 at 60 K, and heating to different temperatures. Directly after Rh deposition at room temperature the shape of the Rh $3d_{5/2}$ peak has a maximum at ≈307.7 eV, but as mentioned previously, its shape suggests convolution of several components. A small shoulder at ≈309.5 eV corresponds to Rh incorporated in the octahedral sites of the support (see Fig. 2); this component can be minimized by depositing Rh at lower temperature (Fig. S5†). After dosing O_2 at 60 K, the maximum of the Rh $3d_{5/2}$ peak shifts by ≈0.9 eV to 308.6 eV. Heating to 300 K induces a further shift to ≈309.0 eV, and this position remains the same with heating to 400 K. At this temperature, a small shoulder at 308.2 eV appears. Heating above 460 K causes growth of the 309.5 eV component corresponding to incorporated Rh and slight increase of the signal at 308.2 eV. Above 700 K only the signal from the incorporated Rh remains. The Fe 2p region does not show any significant changes with O_2 adsorption and heating (spectra shown in Fig. S6†). The question of how the changes in XPS spectra correlate to the O_2-induced Rh_1 agglomeration observed by STM is covered in the discussion section.

Exposing $Rh_1/Fe_3O_4(001)$ to CO

The same experimental approach as utilized above for O_2 was used to study CO adsorption on the Rh_1 adatoms. Fig. 5 shows five frames of an STM movie recorded while keeping a background pressure of 5×10^{-9} mbar CO in the analysis chamber. In panel (a), the vast majority of the Rh_1 species have an apparent height of ≈180 pm (red circle). Over the course of the movie, the apparent height of the individual Rh_1 species abruptly decreases to 95–125 pm (panels b–d) and eventually almost all of the Rh_1 appear darker (panel (e)). We attribute this change to the formation of monocarbonyl RhCO, and the reduction of the apparent height to the modification of empty Rh states near the Fermi level through the interaction with CO. With higher doses of CO, we also observe double-lobed species oriented perpendicular to the surface Fe rows, which we assign as $Rh(CO)_2$ dicarbonyls (orange arrow in Fig. 5e and Fig. S7†). Noncontact atomic force microscopy (ncAFM) measurements of the Rh carbonyls acquired with a CO-terminated tip (Fig. S7†) appear strikingly
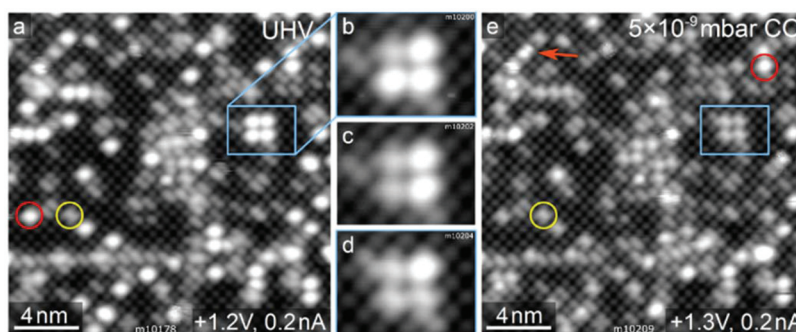

Fig. 5 Adsorption of CO on the $Rh_1/Fe_3O_4(001)$ followed by STM. In panel (a), acquired in UHV, the vast majority of the Rh_1 adatoms (red circle) have an apparent height of ≈180 pm. (b–d) During exposure in 5×10^{-9} mbar CO, the individual Rh_1 change their apparent height one by one to ≈95–125 pm. We identify these as $Rh_1(CO)$ species. (e) After a CO dose of ≈10 L, the majority of Rh_1 are darker. The images also show a few double-lobed features (orange arrow), which we attribute to $Rh_1(CO)_2$ dicarbonyls. Detailed images of these species are shown in Fig. S5.†

similar to those observed in the previously published study of $Ir_1/Fe_3O_4(001)$,[14] and one would indeed expect similar behavior for these two metals. As in the Ir case, the concentration of the dicarbonyl species never exceeded 25% of the total, which we attribute to the low pressures used in our experiments. Neither the monocarbonyls nor dicarbonyls appear to interact with molecular O_2, as no changes were observed upon subsequent O_2 exposure in room-temperature STM measurements.

In ^{13}CO TPD experiments on 0.5 ML $Rh/Fe_3O_4(001)$, we observe a ^{13}CO desorption peak with a maximum at ≈530 K, which has an additional shoulder at ≈450 K (Fig. 6a). Comparison to the spectrum acquired on the pristine $Fe_3O_4(001)$ reveals that all the desorption signal above 250 K is
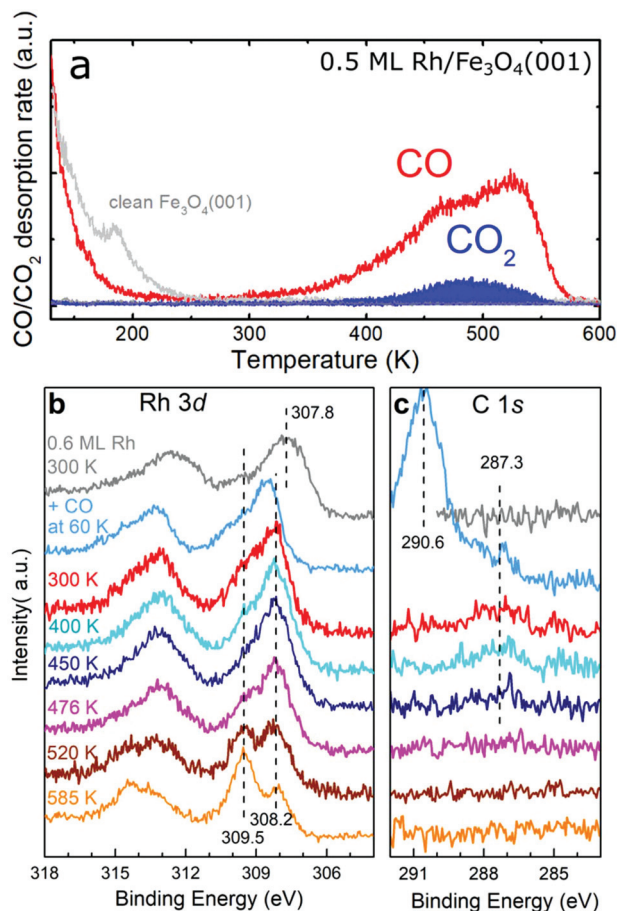

Fig. 6 TPD and XPS characterization of CO adsorbed on Rh/ $Fe_3O_4(001)$. (a) CO desorbs from 0.5 ML $Rh/Fe_3O_4(001)$ in a peak with a maximum around 530 K. A smaller signal of CO_2 is observed peaking around 480 K. (b) Adsorption of CO at 60 K on 0.6 ML $Rh/Fe_3O_4(001)$ shifts the Rh 3d photoemission peak maximum to 308.5 eV, but heating to 300 K shifts the maximum to 308.2 eV. With annealing to temperatures above 500 K, a new component develops at 309.5 eV, due to Rh incorporated into the $Fe_3O_4(001)$ support. (c) In the C 1s region of the XPS spectra, adsorption of CO at 60 K results in a dominant feature at 290.6 eV, corresponding to CO adsorbed at the $Fe_3O_4(001)$ surface,[32] and a smaller peak at 287.3 eV, corresponding to CO adsorbed on the Rh species. The 287.3 eV component is still observed after heating to 450 K. Above this temperature, no C 1s signal is observed in XPS.

related to Rh, and that the presence of Rh leads to disappearance of a defect-related ^{13}CO desorption peak at ≈190 K. On $Rh/Fe_3O_4(001)$, a small $^{13}CO_2$ signal is observed at ≈480 K, which we attribute to CO oxidation via a Mars-van-Krevelen mechanism. This phenomenon has been observed for Ir single atoms and Pt clusters on $Fe_3O_4(001)$.[14,18] No CO desorption is observed above 580 K and in XPS spectra the C 1s region is featureless after heating to these temperatures (Fig. 6c). The CO desorption features below 200 K in the TPD spectra correspond to CO adsorption on the clean $Fe_3O_4(001)$ surface.[32] Focusing on the Rh 3d and C 1s regions of the XPS spectra, CO adsorption at 60 K induced a shift of the Rh 3d peak maximum to 308.5 eV accompanied by the emergence of C 1s peak components at 290.6 eV and 287.3 eV. The 290.6 eV peak corresponds to adsorption of CO on the bare $Fe_3O_4(001)$ surface.[32] Heating to 300 K leads to desorption of CO from $Fe_3O_4(001)$, so that only CO bound to the Rh species remains (287.3 eV component in the C 1s region). The Rh 3d peak maximum shifts to lower binding energy (308.2 eV), and this position stays constant upon heating to higher temperatures. After the CO desorption from the Rh species above ≈500 K, the majority of the Rh incorporates into the surface, clearly evidenced by the increase in intensity of the component at 309.5 eV. Repeated ^{13}CO TPD measurements feature a small desorption peak at ≈410 K (Fig. S8†), which we attribute to CO desorption from Rh_1 substituting an Fe atom in the 5-fold surface site. The Fe 2p region of the XPS spectra taken after CO adsorption and heating to different temperatures shows the same shape as the spectra taken without the CO (see Fig. 2c and Fig. S6†).

Sequential dosing experiments

Sequential ^{13}CO and $^{18}O_2$ dosing experiments were performed to find out whether the Rh adatoms or Rh_xO_y clusters can co-adsorb CO and O_2. Fig. 7a–d shows the CO (red) and CO_2 (blue and orange) signals desorbing from a 0.5 ML $Rh/Fe_3O_4(001)$ sample exposed to CO and O_2 at different temperatures and in a different order. The blue area corresponds to CO_2 formed via a MvK mechanism ($^{13}C^{16}O_2$, mass 45), while the orange area indicates CO_2 formed by a L–H mechanism ($^{13}C^{16}O^{18}O$, mass 47). The corresponding $^{18}O_2$ signal (mass 36) acquired simultaneously is shown in Fig. S9.† Fig. 7a provides a reference in which the sample was saturated by ^{13}CO at 300 K. Dosing O_2 on the sample predosed with ^{13}CO at 130 K (panel b) leads to a lower CO desorption signal, and the overall amount of CO_2 produced is increased. The CO_2 signal produced via a MvK mechanism is comparable to the previous case, but additionally we observe a low, broad $^{13}C^{16}O^{18}O$ signal between 200–500 K corresponding to CO_2 formed by a L–H mechanism. Overall, roughly 35% of the CO_2 produced is formed by the L–H channel.

The situation changes dramatically when the same gases are dosed with the order reversed (panel c). Dosing the $^{18}O_2$ before the ^{13}CO at 130 K leads to a significantly enhanced mass 47 signal, which now exhibits a clear maximum at ≈340 K. The sum of masses 29, 45 and 47 is however signifi-
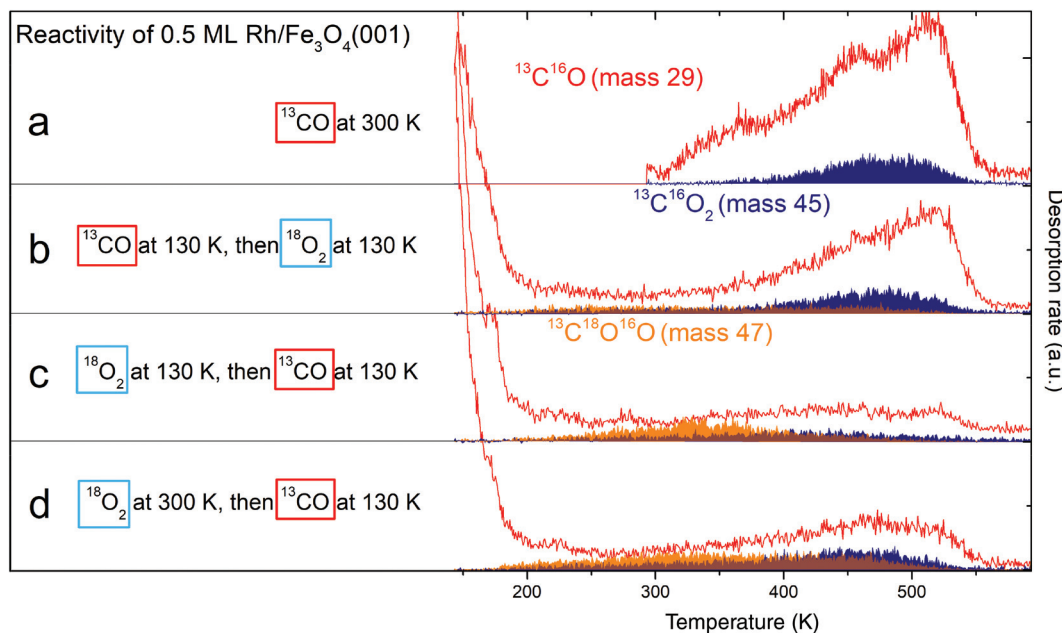
Fig. 7 Probing the reactivity of 0.5 ML Rh/Fe$_3$O$_4$(001) by TPD after sequential dosing of ^{13}CO and ^{18}O$_2$. Red traces correspond to ^{13}CO, blue areas to ^{13}C^{16}O$_2$ produced *via* a MvK mechanism and orange areas correspond to ^{13}C^{16}O^{18}O produced *via* a L–H mechanism. (a) Dosing ^{13}CO at 300 K results in spectra comparable to Fig. 6a. (b) Dosing ^{13}CO at 130 K, then ^{18}O$_2$ at 130 K leads to a lower ^{13}CO desorption signal, but overall higher ^{13}CO$_2$ production below 400 K. (c) Dosing ^{18}O$_2$ first at 130 K, then ^{13}CO at 130 K leads to significant CO$_2$ signal produced by the L–H mechanism, the MvK channel is suppressed. (d) Dosing ^{18}O$_2$ at 300 K, then ^{13}CO at 130 K leads to similar results as (c), but with more CO$_2$ produced above 400 K in both reaction channels.

cantly reduced compared to the previous CO-first experiments, which suggests that, overall, less CO can adsorb on the system once it is saturated with O$_2$ at 130 K, but a significantly higher proportion of adsorbed CO is converted to CO$_2$. The overall amount of CO$_2$ produced is comparable to the case shown in Fig. 7b, but now the majority ($\approx$60%) forms *via* the L–H channel. If the system is predosed with O$_2$ at 300 K prior to CO adsorption, the observed CO$_2$ TPD signal shown in Fig. 7d is significantly enhanced between 400 and 500 K in both reaction channels. In this experiment the amount of formed CO$_2$ is the highest ($\approx$35% higher than in the previous two cases), and approximately 50% is formed by the L–H channel. These experiments, with O$_2$ predosing at 130 and 300 K, likely differ in that the oxygen-induced Rh$_1$ diffusion should be suppressed at low temperature, and additional oxygen is bound at sites linked to Rh species (see Fig. 4a). No CO$_2$ formation by any mechanism is observed in the absence of Rh species (see Fig. S10†).

Discussion

The experimental data acquired on the Rh/Fe$_3$O$_4$(001) model catalyst clearly show that Rh$_1$ adatoms sinter rapidly when exposed to O$_2$ at room temperature, forming small Rh$_x$O$_y$ clusters that are active for CO oxidation. Given the extremely low O$_2$ pressure used in the STM movies, it seems likely that just

one O$_2$ molecule is sufficient to create a mobile oxidised Rh species, probably Rh$_1$O$_2$. This suggests that oxygen adsorption significantly weakens the interaction of the Rh adatom with the support. DFT calculations for oxygen adsorption on the Rh$_1$/Al$_2$O$_3$ system predict significant electron transfer from Rh to O$_2$, and the formation of superoxo (O$_2$)$^-$ species.[3] In the O 1s XPS data taken after O$_2$ adsorption below 100 K (Fig. 4b) we do observe a peak at 533.7 eV, which is close to the position expected for superoxo species.[33] However, this peak disappears after heating above 250 K, suggesting a further reaction with Rh takes place. We also observe a strong positive binding energy shift in the Rh 3d XPS peak maximum (Fig. 4c) after O$_2$ dosing at 60 K (308.6 eV), which shifts further to $\approx$309.0 eV upon heating above 250 K. Even though the position observed at 60 K is already close to that expected for RhO$_2$ (308.6 eV)[34] or Rh$_2$O$_3$ (308.3 eV),[34,35] and thus could be already interpreted as a signal corresponding to the oxidised Rh clusters, the further shift above 250 K accompanied with the disappearance of the superoxo component in the O 1s region suggests that the agglomeration takes place between 100 K and 250 K, and the O 1s signal of the resulting Rh$_x$O$_y$ nanoparticles is indistinguishable from that of the O^{2-} in the Fe$_3$O$_4$ support.

Our room-temperature STM movies of O$_2$ exposure (Fig. 3a–c) suggest that the mobile Rh$_1$O$_2$ species interact strongly with bare Rh adatoms to form a well-defined double protrusion (presumably with Rh$_2$O$_2$ stoichiometry). The addition of yet another mobile Rh$_1$O$_2$ seems common, and would in principle

yield clusters of nominal Rh_3O_4 stoichiometry. These clusters appear larger, and have a scratchy appearance due to the interaction with the STM tip. The cluster density observed following 50 L O_2 exposure suggests that the clusters rarely grow larger than 2–3 Rh atoms, but it cannot be concluded how many O_2 molecules can ultimately be adsorbed on each cluster, nor whether the formation of these clusters results in the abstraction of one or more O atoms. Nevertheless, the O_2 TPD measurements clearly show that some of the O atoms are weakly bound, and desorb as molecular O_2 just above room temperature in the absence of CO (Fig. 4a). The Rh 3d spectrum is barely changed by this desorption; only a very small shoulder appears at ≈308.2 eV (green curve in Fig. 4c), which suggests the clusters remain oxidised. This shoulder gets significantly more pronounced after heating to 460 and 575 K (purple and cyan curves in Fig. 4c), and at the same time the component corresponding to incorporated Rh appears (309.5 eV). In the TPD spectra there is no O_2 desorption signal observed above 380 K (up to 660 K, where the acquisition was stopped), therefore it seems likely that the oxygen from Rh_xO_y clusters gets accommodated in the Fe_3O_4 lattice as the Rh incorporates, and the 308.2 eV component in this case indicates an intermediate step between Rh_xO_y on the surface and Rh incorporated in the lattice. Repeating the oxygen exposure (after its desorption at ≈350 K, but before the Rh incorporation at higher temperatures) does not replenish the weakly bound O_2, suggesting that the clusters restructure to a stable configuration, and that the weakly bound oxygen was a consequence of the agglomeration process.

When the O_2-sintered sample is exposed to CO at low temperature and TPD is performed, CO_2 is found to evolve from the sample in a broad signal between 200–500 K (Fig. 7d). Isotopic labelling of the reactants shows that the majority of the CO_2 formed below ≈400 K is produced by the L–H channel, with the molecular O_2 being the oxidising agent. The observation of a similar result when the initial O_2 exposure was performed at 130 K instead of 300 K hints that O_2-induced sintering happens already at low temperatures. Interestingly, the CO_2 signal at higher temperature is reduced in intensity when the O_2 exposure is performed at 130 K. The comparison of these two datasets suggests that the oxygen bound above 300 K (δ peak in Fig. 4a) is facilitating the CO_2 formation by the L–H channel, and the oxygen adsorbed below 300 K likely blocks a small number of sites for CO adsorption. An alternative explanation is that at 300 K the $^{18}O_2$ spills over to the Fe_3O_4 surface, which leads to the increased CO_2 production above 400 K. In this case the process would be MvK, but due to the previous spillover from Rh it would be measured in both $^{13}C^{16}O_2$ and $^{13}C^{16}O^{18}O$ signals. Reexposing the surface to O_2 following CO_2 desorption is not expected to facilitate further CO_2 production via a L–H mechanism, because the remaining Rh_xO_y clusters seem to be inert for further interaction with O_2.

When the $Rh_1/Fe_3O_4(001)$ sample is exposed to CO first, the Rh adatoms do not become mobile at room temperature. We have recently shown that CO adsorption allows Ir_1 adatoms to achieve highly-stable square-planar environments,[14] and our STM/ncAFM images for Rh_1 (Fig. S7†) appear very similar. In ref. 14, the enhanced stability was rationalized by analogy to Ir(I) complexes, and it seems reasonable to expect similar behavior for Rh(I), which can also adopt the preferred square planar d^8 configuration. The XPS spectra acquired on the CO-saturated $Rh/Fe_3O_4(001)$ system show almost no change in the Rh 3d region when heated to temperatures between 300 K and 450 K, suggesting most of the Rh carbonyls still exist at 450 K, and are still present before the CO_2 production takes place via a MvK mechanism at ≈480 K. Exposing the CO-saturated sample to O_2 does not lead to visible changes in STM or XPS, nor does it lead to significant low-temperature CO_2 production. We conclude that CO poisons the Rh adatoms for O_2 adsorption, at least under our low-pressure conditions. We thus do not form OCOO species, which have been proposed as possible intermediates in prior studies of CO oxidation by Rh-based single-atom catalysts.[36,37] This could be because the Rh atom is inaccessible to the O_2 molecule once the CO is present, or because adsorbing both molecules on the same Rh adatom is energetically unfavourable. The situation could be different at higher pressures where the kinetic limitations are more easily overcome. A more likely scenario, however, is that stable $Rh(CO)_2$ dicarbonyls would be formed and the catalyst would remain poisoned for CO oxidation via a L–H mechanism. Our TPD experiments show that a small amount of CO is oxidised to CO_2 at high temperature via a MvK mechanism, but this is followed by immediate incorporation of Rh into the support, which ultimately deactivates the catalyst.

Conclusions

This study presents an atomic-scale view on a range of phenomena relevant for heterogeneous catalysis by single atoms and sub-nano clusters. We show that O_2 adsorption initially leads to formation of superoxo species bound to Rh_1 adatoms, which already at room temperature rapidly agglomerate to small Rh_xO_y clusters. CO adsorption, on the other hand, completes the preferred square-planar coordination environment of the Rh_1 adatoms, stabilizing the Rh_1 in place while poisoning them for O_2 adsorption. Both the oxidised Rh_xO_y clusters and Rh_1CO carbonyls show activity for CO oxidation, but via very different pathways: oxidised clusters catalyse the reaction via a Langmuir–Hinshelwood mechanism at temperatures as low as 200 K, while the presence of Rh carbonyls at 300 K allows CO_2 formation via a Mars-van-Krevelen mechanism at ≈480 K. These results highlight the importance of a careful characterization of the catalyst during the exposure to the reactants and show that the gas composition can play a crucial role in the structural evolution of the catalyst.

Conflicts of interest

There are no conflicts to declare.

Acknowledgements

References

1 H. Guan, J. Lin, B. Qiao, X. Yang, L. Li, S. Miao, et al., Catalytically Active Rh Sub-Nanoclusters on TiO2 for CO Oxidation at Cryogenic Temperatures, Angew. Chem., Int. Ed., 2016, 55(8), 2820–2824.

2 J. C. Matsubu, S. Zhang, L. DeRita, N. S. Marinkovic, J. G. Chen, G. W. Graham, et al., Adsorbate-mediated strong metal–support interactions in oxide-supported Rh catalysts, Nat. Chem., 2016, 9, 120.

3 T. K. Ghosh and N. N. Nair, Rh_1/γ-Al_2O_3 Single-Atom Catalysis of O_2 Activation and CO Oxidation: Mechanism, Effects of Hydration, Oxidation State, and Cluster Size, ChemCatChem, 2013, 5(7), 1811–1821.

4 J. Gustafson, O. Balmes, C. Zhang, M. Shipilin, A. Schaefer, B. Hagman, et al., The Role of Oxides in Catalytic CO Oxidation over Rhodium and Palladium, ACS Catal., 2018, 8(5), 4438–4445.

5 G. S. Parkinson, Iron oxide surfaces, Surf. Sci. Rep., 2016, 71(1), 272–365.

6 H.-J. Freund, G. Meijer, M. Scheffler, R. Schlögl and M. Wolf, CO Oxidation as a Prototypical Reaction for Heterogeneous Processes, Angew. Chem., Int. Ed., 2011, 50(43), 10064–10094.

7 A. Beniya and S. Higashi, Towards dense single-atom catalysts for future automotive applications, Nat. Catal., 2019, 2(7), 590–602.

8 S. Sinthika, S. T. Vala, Y. Kawazoe and R. Thapa, CO Oxidation Prefers the Eley–Rideal or Langmuir–Hinshelwood Pathway: Monolayer vs Thin Film of SiC, ACS Appl. Mater. Interfaces, 2016, 8(8), 5290–5299.

9 M. A. Newton, D. Ferri, G. Smolentsev, V. Marchionni and M. Nachtegaal, Room-temperature carbon monoxide oxidation by oxygen over Pt/Al_2O_3 mediated by reactive platinum carbonates, Nat. Commun., 2015, 6, 8675.

10 Q. Pan, X. Weng, M. Chen, L. Giordano, G. Pacchioni, C. Noguera, et al., Enhanced CO Oxidation on the Oxide/Metal Interface: From Ultra-High Vacuum to Near-Atmospheric Pressures, ChemCatChem, 2015, 7(17), 2620–2627.

11 Y. Lu, J. Wang, L. Yu, L. Kovarik, X. Zhang, A. S. Hoffman, et al., Identification of the active complex for CO oxidation over single-atom Ir-on-$MgAl_2O_4$ catalysts, Nat. Catal., 2019, 2(2), 149–156.

12 A. Halder, L. A. Curtiss, A. Fortunelli and S. Vajda, Perspective: Size selected clusters for catalysis and electrochemistry, J. Chem. Phys., 2018, 148(11), 110901.

13 P. T. P. Ryan, Z. Jakub, J. Balajka, J. Hulva, M. Meier, J. T. Küchle, et al., Direct measurement of Ni incorporation into Fe_3O_4(001), Phys. Chem. Chem. Phys., 2018, 20(24), 16469–16476.

14 Z. Jakub, J. Hulva, M. Meier, R. Bliem, F. Kraushofer, M. Setvin, et al., Local Structure and Coordination Define Adsorption in a Model Ir_1/Fe_3O_4 Single-Atom Catalyst, Angew. Chem., Int. Ed., 2019, 58(39), 13961–13968.

15 R. Bliem, J. Pavelec, O. Gamba, E. McDermott, Z. M. Wang, S. Gerhold, et al., Adsorption and incorporation of transition metals at the magnetite Fe_3O_4(001) surface, Phys. Rev. B: Condens. Matter Mater. Phys., 2015, 92(7), 075440.

16 L. DeRita, J. Resasco, S. Dai, A. Boubnov, H. V. Thang, A. S. Hoffman, et al., Structural evolution of atomically dispersed Pt catalysts dictates reactivity, Nat. Mater., 2019, 18(7), 746–751.

17 K. Zhao, H. Tang, B. Qiao, L. Li and J. Wang, High Activity of Au/γ-Fe_2O_3 for CO Oxidation: Effect of Support Crystal Phase in Catalyst Design, ACS Catal., 2015, 5(6), 3528–3539.

18 R. Bliem, J. van der Hoeven, A. Zavodny, O. Gamba, J. Pavelec, P. E. de Jongh, et al., An Atomic-Scale View of CO and H_2 Oxidation on a Pt/Fe_3O_4 Model Catalyst, Angew. Chem., Int. Ed., 2015, 54(47), 13999–14002.

19 D. Widmann and R. J. Behm, Active Oxygen on a Au/TiO_2 Catalyst: Formation, Stability, and CO Oxidation Activity, Angew. Chem., Int. Ed., 2011, 50(43), 10241–10245.

20 K. Zhang, S. Shaikhutdinov and H.-J. Freund, Does the Surface Structure of Oxide Affect the Strong Metal–Support Interaction with Platinum? Platinum on Fe_3O_4(001) versus Fe_3O_4(111), ChemCatChem, 2015, 7(22), 3725–3730.

21 G. S. Parkinson, Z. Novotny, G. Argentero, M. Schmid, J. Pavelec, R. Kosak, et al., Carbon monoxide-induced adatom sintering in a Pd–Fe_3O_4 model catalyst, Nat. Mater., 2013, 12(8), 724–728.

22 J. I. J. Choi, W. Mayr-Schmölzer, F. Mittendorfer, J. Redinger, U. Diebold and M. Schmid, The growth of ultra-thin zirconia films on Pd_3Zr(0001), J. Phys.: Condens. Matter, 2014, 26(22), 225003.

23 J. Pavelec, J. Hulva, D. Halwidl, R. Bliem, O. Gamba, Z. Jakub, et al., A multi-technique study of CO_2 adsorption on Fe_3O_4 magnetite, J. Chem. Phys., 2017, 146(1), 014701.

24 R. Bliem, E. McDermott, P. Ferstl, M. Setvin, O. Gamba, J. Pavelec, et al., Subsurface cation vacancy stabilization of the magnetite (001) surface, Science, 2014, 346(6214), 1215–1218.

25 B. Arndt, R. Bliem, O. Gamba, J. E. S. van der Hoeven, H. Noei, U. Diebold, et al., Atomic structure and stability of magnetite Fe_3O_4(001): An X-ray view, Surf. Sci., 2016, 653, 76–81.

26 Z. Novotný, G. Argentero, Z. Wang, M. Schmid, U. Diebold and G. S. Parkinson, Ordered Array of Single Adatoms with Remarkable Thermal Stability: Au/Fe_3O_4(001), Phys. Rev. Lett., 2012, 108(21), 216103.

27 R. Bliem, R. Kosak, L. Perneczky, Z. Novotny, O. Gamba, D. Fobes, et al., Cluster Nucleation and Growth from a Highly Supersaturated Adatom Phase: Silver on Magnetite, ACS Nano, 2014, 8(7), 7531–7537.

28 M. Meier, Z. Jakub, J. Balajka, J. Hulva, R. Bliem, P. K. Thakur, *et al.*, Probing the geometry of copper and silver adatoms on magnetite: quantitative experiment versus theory, *Nanoscale*, 2018, **10**(5), 2226–2230.

29 R. Gargallo-Caballero, L. Martin-Garcia, A. Quesada, C. Granados-Miralles, M. Foerster, L. Aballe, *et al.*, Co on Fe_3O_4(001): Towards precise control of surface properties, *J. Chem. Phys.*, 2016, **144**(9), 094704.

30 A. P. Grosvenor, B. A. Kobe, M. C. Biesinger and N. S. McIntyre, Investigation of multiplet splitting of Fe 2p XPS spectra and bonding in iron compounds, *Surf. Interface Anal.*, 2004, **36**(12), 1564–1574.

31 M. Meier, J. Hulva, Z. Jakub, J. Pavelec, M. Setvin, R. Bliem, *et al.*, Water agglomerates on Fe_3O_4(001), *Proc. Natl. Acad. Sci. U. S. A.*, 2018, **115**, E5642–E5E50.

32 J. Hulva, Z. Jakub, Z. Novotny, N. Johansson, J. Knudsen, J. Schnadt, *et al.*, Adsorption of CO on the Fe_3O_4(001) surface, *J. Phys. Chem. B*, 2018, **122**(2), 721–729.

33 D. Halwidl, W. Mayr-Schmölzer, M. Setvin, D. Fobes, J. Peng, Z. Mao, *et al.*, A full monolayer of superoxide: oxygen activation on the unmodified $Ca_3Ru_2O_7$(001) surface, *J. Mater. Chem. A*, 2018, **6**(14), 5703–5713.

34 Y. Abe, K. Kato, M. Kawamura and K. Sasaki, Rhodium and Rhodium Oxide Thin Films Characterized by XPS, *Surf. Sci. Spectra*, 2001, **8**(2), 117–125.

35 S. Blomberg, E. Lundgren, R. Westerström, E. Erdogan, N. M. Martin, A. Mikkelsen, *et al.*, Structure of the Rh_2O_3(0001) surface, *Surf. Sci.*, 2012, **606**(17), 1416–1421.

36 F. Li, Y. Li, X. C. Zeng and Z. Chen, Exploration of High-Performance Single-Atom Catalysts on Support M_1/FeO_x for CO Oxidation via Computational Study, *ACS Catal.*, 2015, **5**(2), 544–552.

37 E. A. Wovchko and J. T. Yates, Activation of O_2 on a Photochemically Generated Rh^I Site on an Al_2O_3 Surface: Low-Temperature O_2 Dissociation and CO Oxidation, *J. Am. Chem. Soc.*, 1998, **120**(40), 10523–10527.